

Research paper

Deformation based additive manufacturing of a metastable high entropy alloy via Additive friction stir deposition

Priyanshi Agrawal ^{a,b,c,1}, Ravi Sankar Haridas ^{a,c,1,2}, Priyanka Agrawal ^{a,c}, Rajiv S. Mishra ^{a,b,c,*}^a Department of Materials Science and Engineering, University of North Texas, Denton, TX 76203, USA^b Center for Agile and Adaptive Additive Manufacturing (CAAAM), University of North Texas, Denton, TX 76207, USA^c Advanced Materials and Manufacturing Processes Institute (AMMPI), University of North Texas, Denton, TX 76207, USA

ARTICLE INFO

ABSTRACT

Keywords:

Additive friction stir deposition
Transformation induced plasticity
High entropy alloys
Microstructural evolution
Dual phase recrystallization kinetics

Additive friction stir deposition (AFSD) is a novel solid-state additive manufacturing process which offers unique capability of producing 3-D parts with no solidification related defects and having homogeneous, equiaxed microstructure. However, to fulfill the full potential of the process for structural applications, AFSD needs intense process optimization for a wide range of alloys with excellent mechanical properties. The present study explored AFSD of a novel metastable high entropy alloy (HEA), CS-HEA ($\text{Fe}_{40}\text{Mn}_{20}\text{Co}_{20}\text{Cr}_{15}\text{Si}_5$ (at%)), enabled with transformation and twinning induced plasticity during deformation. Intense shear deformation at elevated temperature and strain rate during AFSD led to the operation of restoration mechanisms such as recovery, recrystallization, and grain growth which resulted in refined grains with excellent strength and work hardenability. The average grain size for as-deposited CS-HEA is $3.0 \pm 0.5 \mu\text{m}$, and the average tensile yield strength of as-deposited CS-HEA is $450 \pm 20 \text{ MPa}$. The microstructural variation and mechanical response of the alloy as a function of process parameters were correlated to the AFSD process variables, phase transformation, and recrystallization kinetics. Further, the interaction between recrystallization kinetics and transformation kinetics on microstructural evolution of the material was explored. Additionally, the microstructure and stacking fault energy of the alloy were used to predict the mechanical response of the deposited material using a five parameter work hardening model.

1. Introduction

Ability to build complex geometries, needless post-fabrication machining operation, applicability to wide range of alloys, and better production rate add to versatility of additive manufacturing (AM) as a metal fabrication process [1–3]. Similar to conventional manufacturing processes, AM processes are either fusion-based or deformation-based [4]. Research on fusion based AM has advanced drastically over the last decade whereas the deformation based AM processes are still in the budding state [5–8]. This study is focused on additive friction stir deposition (AFSD), a deformation based solid-state AM process. AFSD process is based on the principles of friction stir heating where the material is 3D deposited via severe plastic deformation at high temperature and strain rate. Coupled action of compression and shear forces at elevated temperature due to friction stir heating and plasticity related

adiabatic heating, enable layer wise deposition of the plasticized material [4,9].

The extreme thermomechanical conditions during AFSD process result in operation of dynamic restoration mechanisms [10]. These dynamic restoration mechanisms can be classified as continuous or discontinuous. Discontinuous mechanisms occur heterogeneously throughout the materials which can be described using nucleation and growth stages, whereas continuous mechanisms occur uniformly with no identifiable nucleation and growth stages. Based on intrinsic material property such as stacking fault energy (SFE), the controlling restoration mechanism can either be continuous or discontinuous. For a high SFE material such as Al, the controlling mechanism will be continuous, which is characterized by dynamic recovery, sub-grain formation which progresses to gradual increase in misorientation with strain. For low SFE materials such as steel, or Ni based superalloys, the operating

* Corresponding author at: Department of Materials Science and Engineering, University of North Texas, Denton, TX 76203, USA.
E-mail address: Rajiv.Mishra@unt.edu (R.S. Mishra).

¹ Authors contributed equally

² Department of Mechanical Engineering, University of North Texas, Denton, TX 76203, USA

mechanism will be discontinuous, where nucleation and growth of the grains take place via high angle grain boundary migration [11–13]. The microstructure evolution during thermomechanical processing in dual phase alloys which exhibits deformation induced transformation is distinct from single phase alloys as phase transformation interacts with inherent recrystallization mechanisms [14–16]. AFSD of high SFE Al alloys is extensively studied where the microstructure is observed to be refined significantly after AFSD. Extensive deformation at elevated temperature during AFSD led to operation of continuous dynamic recrystallization in the material. Additionally, our previous study on microstructure evolution during AFSD of low SFE SS316 resulted in grain refinement due to operation of discontinuous dynamic recrystallization mechanisms [10].

Recently, efforts towards expanding the material inventory for AFSD have been reported. High entropy alloys (HEAs), owing to their good synergistic mechanical properties [17,18] and high corrosion resistance [19] have become attractive for potential structural applications. Vast compositional space and microstructural flexibility offered by HEAs can be utilized to design a new alloy system for AFSD. Exploration of vast compositional space enabled development of HEAs with wide range of mechanical properties. Additionally, variation of single alloying element substantially varied the phase stability of the material [20,21]. Guidelines to control the metastability of phases in HEAs by activating multiple deformation mechanisms in HEAs to achieve excellent strength and work hardening have been discussed in detail [18,22]. SFE is the main criteria of activate TRIP/TWIP effect in the HEAs, which is mainly achieved by tuning the composition of equiatomic HEAs [23,24]. One additional design aspect is to add minor alloying elements to reduce the SFE of the alloy [24]. Alloys with low SFE enable activation of twinning induced plasticity (TWIP) or transformation induced plasticity (TRIP) under deformation, thereby results in enhanced strength and ductility. Following the HEA design strategy [18,22,25], a novel Fe₄₀Mn₂₀Co₂₀Cr₁₅Si₅ (at%) TRIP HEA (CS-HEA) with very low SFE has been developed [22,26], Fe₄₀Mn₂₀Co₂₀Cr₁₅Si₅ (at%) alloy named as CS-HEA because Co and Si were added to enhance the metastability of the alloy. Effect of addition of Si on the microstructure of HEAs has been studied in the literature as well, where BCC phase stabilized in AlCoCrCuFeNiSix HEA with the addition of Si [27,28]. Previous studies on the alloy reported a dual phase γ (FCC) and ε (HCP) microstructure and the ability to control the phase stability and microstructure as a function of strain, strain rate, and temperature during processing [29–32]. Such microstructural control with thermo-mechanical processing and excellent strength-ductility-work hardening synergy in the alloy motivated us to explore the potential of the alloy for AFSD. Activation of multiple deformation mechanisms such as deformation induced $\gamma \rightarrow \varepsilon$ transformation, partitioning of plastic strain among γ and ε phases assisted by non-basal slip and twinning in newly-formed ε phase was observed.

In order to take advantage of HEA alloy design strategy for developing specific alloys for AFSD, this study explored the viability of AFSD for TRIP enabled CS-HEA. Process-microstructure-property correlation of CS-HEA fabricated by AFSD was examined in detail. Being a dual phase alloy, the recrystallization behavior, and interaction of transformation and recrystallization mechanisms is discussed in detail for the alloy. Additionally, SFE value of the alloy as a function of microstructure is utilized in a five parameter work hardening model developed by Haridas et al. [33,34] to predict the work hardening behavior of the alloy.

2. Experimental

The AFSD of CS-HEA was performed on MELD-B8® machine using a W-La₂O₃ tool with an outer diameter of 38.1 mm and a total tool length of 88.9 mm. The feedstock material for AFSD of CS-HEA was procured from Sophisticated Alloys Inc. Each feedstock rod used for the deposition was 152 mm long with a square cross-sectional area of 9.52 × 9.52 mm². The feedstock material was fed through the hollow rotating tool and was

plasticized at high temperature by the combined action of friction stir heating and deformation induced (adiabatic) heating. AFSD process was carried out at different tool rotation rates (ω) and tool traverse speeds (v) to vary the heat input during deposition, keeping other parameters such as actuator feed and layer thickness constant. The parameters used for deposition is given in Table 1.

Microscopic characterization was performed at various length scales to understand microstructural evolution of the material. Samples for the characterization were prepared using a KENT USA® electrical discharge machining (EDM). Samples for microscopy were taken from the plane parallel to the build direction, Fig. 1(a) shows the location of the samples for microscopy. The samples were metallographically polished to 0.02 μm to eliminate the effect of surface roughness and to achieve a mirror-like surface finish. The overall microstructural examination was performed using scanning electron microscopy FEI™ Quanta-3D FEG (field emission gun). Electron backscattered diffraction (EBSD) scans were conducted on a SEM FEI™ Nova-Nano SEM 230 equipped with Hikari EBSD detector operating at 20 kV and 6.1 nA current. For large-area EBSD scans, an area of ~ 2 mm × 2 mm was considered at a step size of 0.6 μm , whereas high magnification EBSD scans were conducted at a step size of 30 nm. Beam and video conditions were kept identical between the scans. The EBSD data was further analyzed using TSL OIM 8 software. Transmission electron microscopy (TEM, FEI Tecnai G2 TF20™ operating at 200 kV and JEOL JEM-3000 F HRTEM operating at 300 kV) was used to characterize the microstructure of the as-deposited material. Samples for TEM were prepared using FEI™ Nova 200 dual beam focused ion beam (FIB) microscope.

Dog bone shaped mini-tensile samples having a gage length of 5 mm, 1.25 mm wide and 1.2 mm thick were machined using EDM. The samples were then polished to a surface finish of 1 μm to remove surface irregularities. Samples were taken from the plane perpendicular to build direction, as height of the build was insufficient to prepare mini-tensile sample from the plane parallel to build direction. Fig. 1(b) shows the location and the geometry of tensile sample relative to the build direction, three tensile samples were taken through the thickness of the build. Tensile testing was performed at room temperature under quasi-static conditions at a strain rate of 10⁻³ s⁻¹ using a custom-made computer-controlled mini tensile testing machine. To ensure statistical accuracy, three samples were tested for each condition.

3. Results

3.1. Thermal parameters during processing

The torque experienced by the actuator during AFSD of CS-HEA is obtained from the machine, and the average torque values are given in Table 2. The power and heat input are functions of the torque experienced and calculated values for these parameters are given in Table 2. As observed in our previous study [10,35], the heat input increases with increase in tool rotation rate and reduces with increase in tool traverse speed. The peak temperature during processing for different parameters is also evaluated using the following equation [36]:

$$\frac{T}{T_m} = K \left(\frac{\omega^2}{v \times 10^4} \right)^{\alpha} \quad (1)$$

Table 1

Parameters used for depositing CS-HEA using AFSD process.

Sample No.	Layer thickness (mm)	No. of layers	Tool rotational rate, ω (RPM)	Traverse rate, v (mm/s)	Filler rate (mm/s)
S1	0.50	10	400	5.08	0.42
S2	0.50	10	400	4.23	0.42
S3	0.50	10	600	5.08	0.42
S4	0.50	10	600	4.23	0.42

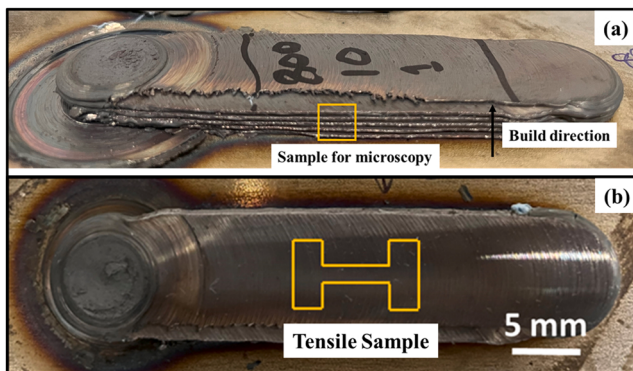


Fig. 1. Images of AFSD deposits of CS-HEA (a) build direction and (b) top view, showing location of samples for microscopy and tensile testing prepared using EDM.

Table 2
Thermal parameters during deposition for AFSD CS-HEA.

Samples	Torque, M (N.m)	Power, P = ($2\pi\alpha M$)/60 (W)	Heat input, Q = P/v (kJ)	Peak temperature (K)
S1	81.98	3432.22	700.52	1194.85
S2	85.00	3558.66	811.40	1202.45
S3	63.49	3987.17	871.28	1229.11
S4	70.48	4426.14	942.59	1236.99

where T_m is the melting temperature for CS-HEA which is ~ 1573 K, calculated from the phase diagram which is plotted using Thermocalc software. The exponent α varies in the range 0.04–0.05, and the value of constant K falls between 0.65 and 0.75.

Since the temperature during AFSD is higher than the martensitic transformation temperature (~ 750 K), interaction of recrystallization and phase transformation may occur. Degree of deformation during AFSD will affect the kinetics of recrystallization as well as transformation. In a recent study it was observed for dual phase steel the nature of the interaction (weak or strong) affects significantly the austenite formation, its spatial distribution, and the resulting

morphology of microstructure [16].

3.2. Microstructural evolution

Warm rolled rods of CS-HEA were used as the base material for AFSD process. The microstructure of the base material is shown in Fig. 2(a-d). Large grains with an average grain size of $50 \pm 25 \mu\text{m}$ with random texture were observed in the material. Microstructure consists of dual phase with 57% γ (f.c.c.)-phase and 43% ϵ (h.c.p)-phase. The conditions during rolling of the base material resulted in the formation of plates of martensitic ϵ -phase in γ matrix. Fig. 2(d) shows the pole figure of the base material, no preferred texture was observed in the material. AFSD is a severe plastic deformation based AM process and the signature microstructure of AFSD shows fine equiaxed grain structure [10,35,37, 38]. Fig. 3(a-d) show the microstructure of metastable CS-HEA 3D-deposited using AFSD at different parameters. Very fine-equiaxed grains with an average size of $\sim 2.0 \pm 1.0 \mu\text{m}$ is observed in as-deposited state. Being a dual phase HEA, the microstructure of as-deposited CS-HEA consisted of both γ and ϵ phases, with higher fraction of ϵ -phase. Pole figures, Fig. 3 (a4-d4) of the as-deposited CS-HEA show no preferred orientation in as-deposited material. Deformation at elevated temperature resulted in operation of dynamic recovery or recrystallization related phenomenon in the AFSD sample. Dynamic recovery/recrystallization resulted in refinement of grains as compared to base material [39]. Additionally, base material showed a γ -phase dominated microstructure whereas the microstructure after AFSD of CS-HEA showed majority of ϵ -phase. Severe plastic strain, thermal cycling, and subsequent cooling during AFSD resulted in $\gamma \rightarrow \epsilon$ transformation during deposition of CS-HEA. In a previous study, we have performed AFSD of single phase austenitic SS316 [10]. Although the process parameters and heat input for deposition is similar for both SS316 and CS-HEA during deposition, as-deposited microstructure differed in both cases; a finer dual-phase microstructure is observed in CS-HEA as compared to SS316. CS-HEA being a dual phase alloy, the recrystallization kinetics differs from SS316 due to a) additional recrystallization sites at phase boundaries, and b) pinning effect exerted by closed packed second phase on both low and high angle boundaries [11].

Fig. 3 shows the comparison of EBSD micrographs of the samples deposited at different AFSD parameters. As discussed above, the heat input as well as peak temperature increases with increase in tool rotation

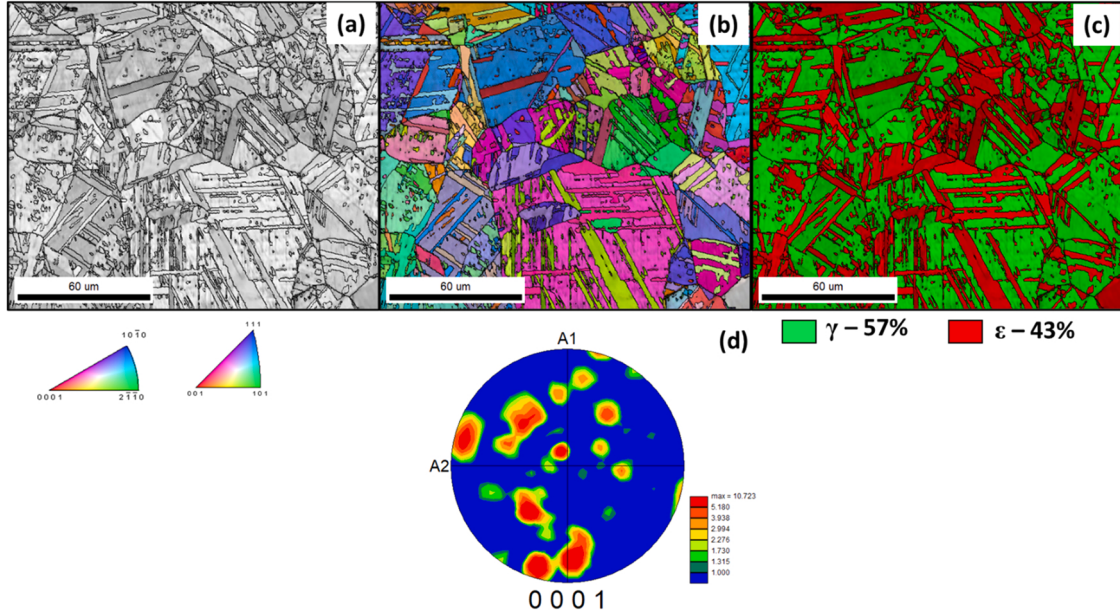


Fig. 2. Microstructure of CS-HEA base material; (a) image quality (IQ) map, (b) inverse pole figure (IPF) map, (c) phase map and (d) pole figure.

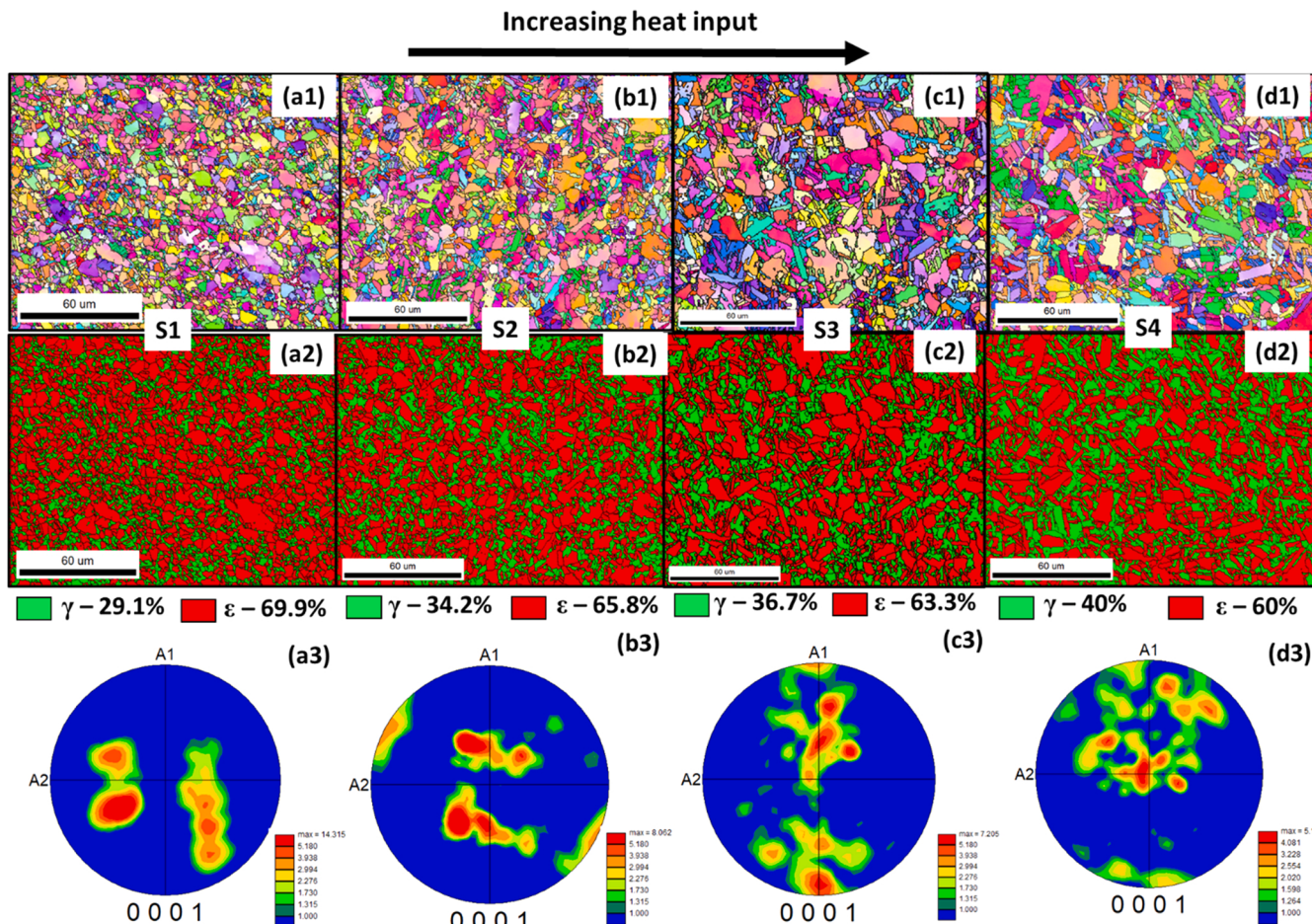


Fig. 3. Inverse pole figure maps, phase maps and pole figures for AFSD deposited samples (a1-a3) S1, (b1-b3) S2, (c1-c3) S3, and (d1-d3) S4, respectively.

Table 3
Average grain size and recrystallization fraction for AFSD CS-HEA.

Samples	S1	S2	S3	S4
Average grain size (μm)	1.75 ± 1.23	2.01 ± 1.53	2.51 ± 2.06	2.53 ± 1.83
Fraction based on KAM	80.3	85.3	90.7	93.7
Fraction based on GOS	76.5	82.2	86.3	91.0

rate. Slower tool traverse speed causes the deposited material to stay at high temperature for an extended time period. Therefore, with increase in peak temperature and extended stay at peak temperature, length scale of microstructural features varies. Sample S1 shows lowest average grain size of $1.75 \pm 1.23 \mu\text{m}$ whereas sample S4 has grains of average grain size of $2.53 \pm 1.83 \mu\text{m}$ (Table 3). Even though the difference in the grain sizes with the change in process parameters is not pronounced, the trend observed is of interest. Phase stability of CS-HEA considerably depends on the processing conditions. In a previous study on friction stir processed CS-HEA, significant dependence of phase stability on processing conditions was observed [29,31]. Therefore, the effect of AFSD processing conditions on phase stability is explored which is shown through phase maps in Fig. 3 (a2-d2). Evidently, AFSD CS-HEA shows dual phase microstructure with a ϵ -phase dominance. Exceptionally low

SFE of CS-HEA and presence of HCP stabilizing elements (Si and Co) lead to stabilization ϵ -phase in the material [40,41]. Moreover, the introduction of strain or chemical energy in the material through processing or slight change in chemical composition significantly affect the phase stability [26,29]. Majority of the base material consists of γ -phase which during AFSD transformed to ϵ -phase due to rapid cooling from elevated temperature. Additionally, Fig. 3 (a2-d2) reveal that the fraction of γ -phase increases with increase in peak temperature/heat input during processing. Both heat input as well as grain size affect the phase stability in metastable HEAs, higher heat input results in increased stability of high temperature γ -phase whereas large grains help in stabilizing ϵ -phase (Eq. 2) [26,33]. In the case of present alloy with changing processing parameters from sample S1 to S4 the heat input increases and so the grain size. As both heat input and grain size have contrary effect on phase stability therefore, the one which dominate will determine the phase evolution with processing parameters. Here, it was observed that γ -phase fraction is increasing from sample S1 to S4 (Fig. 3) therefore heat input is determining the phase stability for the present alloy,

$$\Delta G_{ex}^{\gamma \rightarrow \epsilon} = -k_1 \exp\left(\frac{-d}{L}\right) \quad (2)$$

In order to understand the transformation mechanism and associated microstructural evolution with processing parameters, TEM was performed on two samples deposited at different tool rotation rates but same tool traverse speed (S2 and S4). Fig. 4(a) and (b) show TEM micrographs for samples S2 and S4, respectively. A very high dislocation

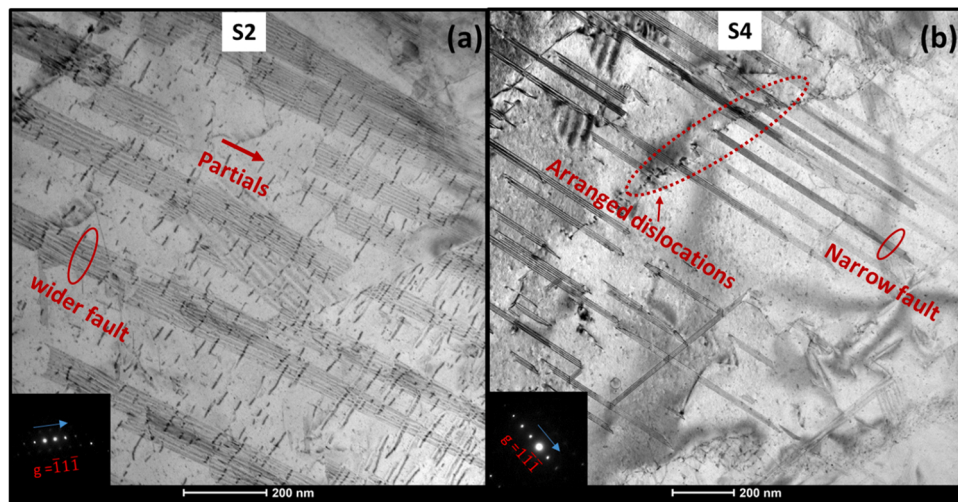


Fig. 4. (a) and (b) bright field TEM micrographs for sample S2 and S4, respectively.

density is observed in both of the samples but relatively higher for sample S2. Moreover, the dislocations are randomly distributed in sample S2 whereas it is arranged in the form of boundary for sample S4, marked in Fig. 4. Lower heat input for sample S2, rendered higher dislocation density. Moreover, the density as well as thickness of the stacking faults is also observed to be higher for sample S2 as compared to sample S4. Stacking faults with a thickness of two planes ($n = 2$) act as a HCP ϵ embryo [42], higher density of wider stacking faults in sample S2 explains the higher ϵ -phase fraction in the sample.

Dynamic recrystallization occurs readily during thermomechanical processing of low SFE materials due to sluggish dynamic recovery as inhibition of climb and cross slip maintain the driving force for recrystallization. Dynamic recrystallization leads to remarkable refinement in the microstructure, hence significant grain refinement is observed in AFSD CS-HEA. During layer-by-layer deposition in AFSD process, the deposited material undergoes multiple deformation and thermal cycles. Such multiple deformation-thermal cycles render partial recrystallization in the material. The fraction of recrystallization estimation is achieved from the EBSD maps of the deposited samples. There are various methods based on which recrystallization fraction can be estimated. Here, we calculated recrystallization fraction using, (a) kernel average misorientation (KAM), and (b) grain orientation spread (GOS). KAM characterizes the local misorientation by averaging the misorientation among the point at the center of the kernel to its nearest neighbors [13]. Strain-free homogenized materials show low KAM values, and hence

recrystallized grains show low KAM values (<1) whereas deformed grains have high KAM values (>1) [43]. GOS is the average difference in the orientation between the average grain orientation and all the measurements in the grain [13]. GOS cutoff of 2.5 was taken in the present study to separate recrystallized grains to deformed grains. KAM and GOS distribution for samples deposited at different parameters using AFSD is given in Fig. 5(a) and (b). The recrystallization fraction is given in Table 3. Recrystallization fraction calculated using KAM is higher when compared to GOS; however, the trend is similar. Samples deposited at higher heat input/temperature shows higher recrystallization fraction.

3.3. Tensile behavior

Tensile testing was performed on AFSD processed CS-HEA to understand the mechanical response of the material. Fig. 6(a) and (b) show engineering stress – strain and work hardening curves for all the samples, respectively. Although AFSD of CS-HEA resulted in a refined microstructure compared to the base material, the yield strength obtained was similar, viz., $\sim 450 \pm 20$ MPa, which is due to the presence of high dislocation density in the warm-rolled base material. The high dislocation density provided significant strengthening to the base material. The ultimate tensile strength (UTS) and ductility of AFSD deposited CS-HEA is ~ 1.5 times the base material. Higher UTS and ductility in AFSD deposited CS-HEA implies higher work hardening rate which is evident from Fig. 6(b). The slope change observed in the work

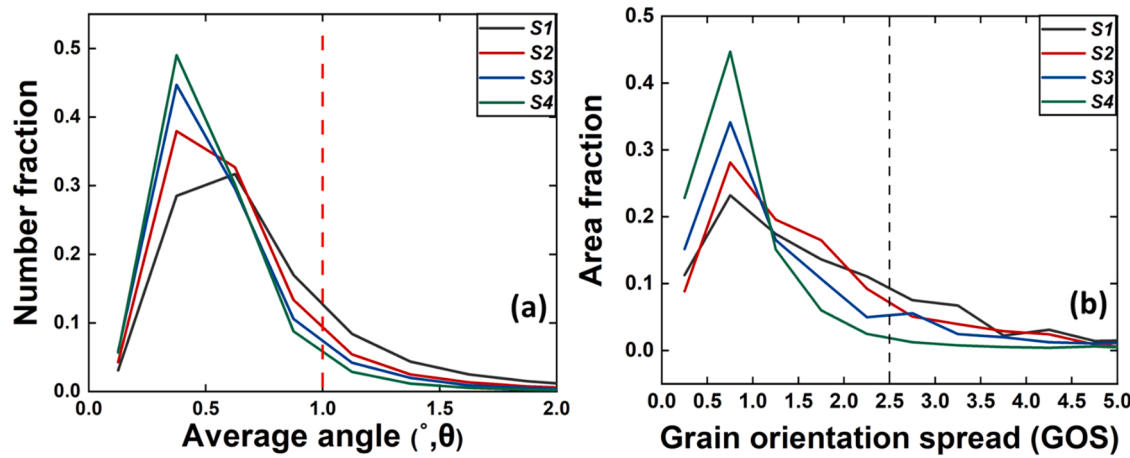


Fig. 5. Recrystallization fraction calculation using EBSD maps; (a) based on Kernel average misorientation, and (a) based on grain orientation spread.

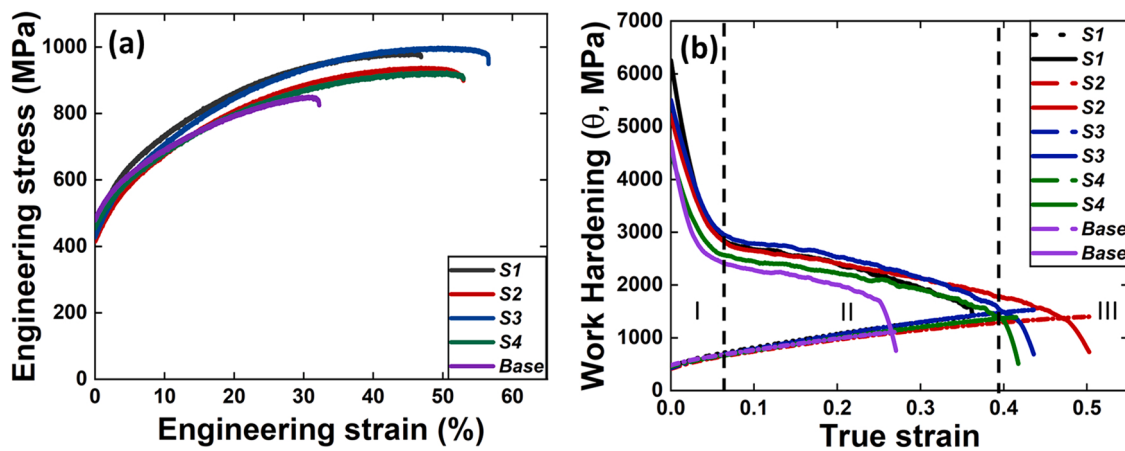


Fig. 6. (a) and (b) engineering stress-strain curves and work hardening curves for all the samples, respectively.

hardening rate curves for both base and AFSD CS-HEA is associated with the change in deformation mechanism [33,34]. The work hardening rate drops drastically in Stage I of deformation (Fig. 6(b)) during which the deformation is dislocation dominant. However, once the stress exceeds the transformation stress, the work hardening rate increases in Stage II of deformation which is characterized by persistent martensitic transformation. Being a low SFE material [30,34], activation of transformation and twinning mechanisms were observed in CS-HEA is our previous studies [6,30,31,33]. Dual phase microstructure in CS HEA promotes strain partitioning between both the phases under deformation [44]. In-situ neutron diffraction studies showed triggering of TRIP in the FCC phase and the activation of single and multiple twinning in the HCP phase due to significant stress redistribution [30,45]. Deformation starts with dislocation activity and stacking fault formation in γ -phase which subsequently progresses to martensitic transformation to ϵ -phase. Further, the deformed as well as the transformed ϵ -phase

undergo deformation by basal slip, non-basal slip, and later by deformation twinning [46,47]. Detailed discussion related to work hardening behavior of the alloy is presented in the discussion section.

4. Discussion

4.1. Recrystallization behavior

As discussed earlier, operation of restoration mechanisms like dynamic recovery and recrystallization lead to the microstructural evolution in thermomechanically processed alloys [4]. In case of low SFE materials, due to difficulty for dislocation climb and cross slip, dynamic recovery is normally not observed [48]. Additionally, dynamic recrystallization mechanisms also dependent on the SFE of the material [49]. Contrary to low SFE materials, propensity of dislocation climb, and cross slip in high SFE materials allow formation of dislocation substructures

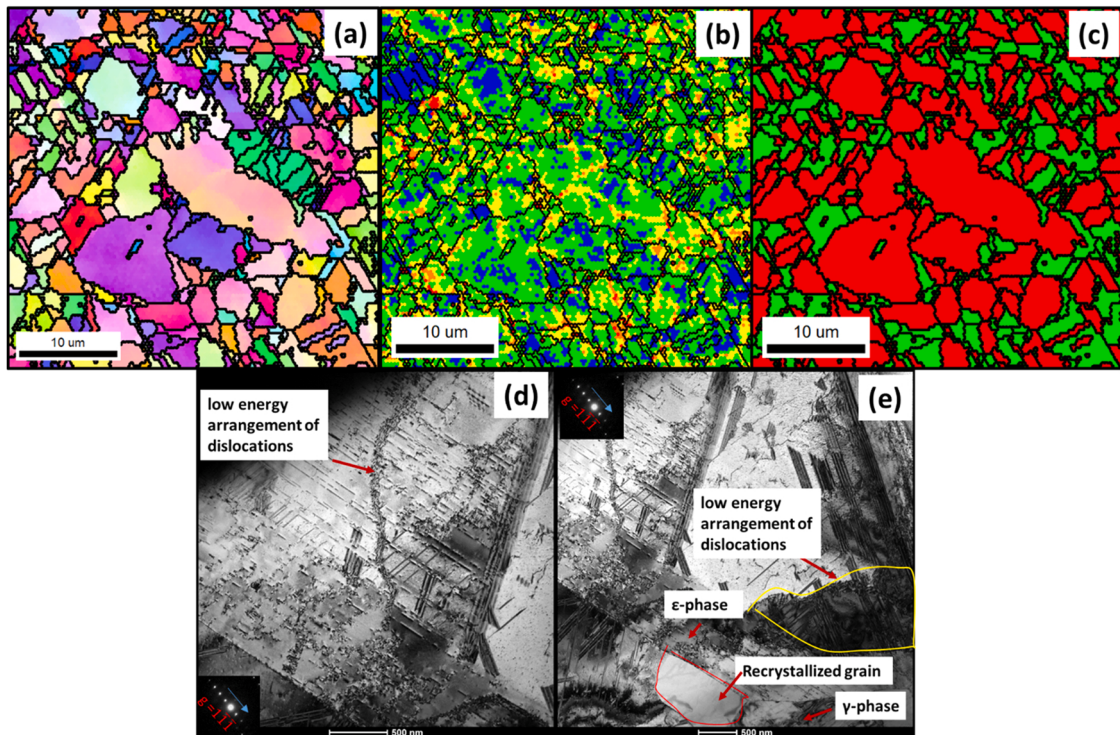


Fig. 7. (a) Inverse pole figure, (b) Kernel average misorientation and (c) phase map for sample S2 respectively, depicting nucleation site for recrystallization; (d) and (e) TEM micrographs for sample S2.

which results in continuous dynamic recrystallization. In the case of low SFE materials, accumulation of dislocations provides the driving force for recrystallization which is associated with high angle boundary migration. Such dynamic recrystallization mechanism has distinct nucleation and growth stages, and hence called discontinuous dynamic recrystallization [11,50]. Significant grain refinement during hot deformation of a TRIP/TWIP HEA was observed in a previous study due to the operation of discontinuous dynamic recrystallization at elevated temperature [51].

In discontinuous dynamic recrystallization, nucleation of new grains is followed by growth of regions depleted in dislocations at the expense of regions with high dislocation accumulation. The nucleation of newly recrystallized grains is one of the key features in discontinuous dynamic recrystallization, and generally grain boundaries act as nucleation sites. During deformation, grain boundary bulging and serration occur which act as a prelude to nucleation, and result in necklace microstructure [49, 50]. However, in the case of dual phase alloys, phase boundaries also act as nucleation sites [14]. Additionally, CS-HEA is a low SFE material with high density of stacking faults (Fig. 4). The stacking faults also aid dynamic recrystallization by providing additional nucleation sites. Fig. 7 (a-c) show EBSD, IPF, KAM, and phase maps of AFSD sample S2 where very fine grains are observed at the boundary of relatively bigger grains. TEM image (Fig. 7(d)) indicates presence of random dislocations, which at specific sites are arranged as dislocation networks. Such dislocation network is a geometrically necessary boundary (GNB) within a deformed grain. In a thermomechanically processed material, the GNBS are generated to ensure the plastic strain compatibility between neighboring grains. Fig. 7(e) shows TEM micrograph where a dislocation free grain is recrystallized at the γ/ϵ phase boundary, which proves the point that phase boundaries also act as a nucleation site.

Abundant nucleation sites available in AFSD CS-HEA in the form of grain boundaries, stacking faults, and phase boundaries promote higher nucleation rate. The nucleated grains impinge each other which restricts the grain growth. Thus, higher nucleation rate with limited grain growth result in finer average grain size in AFSD CS-HEA. Additionally, the nucleation of new grains at the grain boundary of older grains resulted in a necklace microstructure in the material (Fig. 7(a)). Also, the KAM map reveals higher strain in the larger grain as compared to newly recrystallized grains.

4.2. Interaction between recrystallization and transformation

The recrystallization kinetics for dual phase alloys is different from single phase alloys as transformation interacts with recrystallization [14]. Two types of interactions are observed; a) weak interaction - where recrystallization is mostly completed before transformation, and b) strong interaction - where both recrystallization and transformation occurs simultaneously [16]. Recrystallization kinetics of dual phase steel is extensively studied in literature and was observed that at higher heating rate or presence of alloying elements prone to segregation leads to strong interaction [52,53]. Rather a heterogeneous microstructure was observed in strong interaction, while it was homogeneous in weak interaction. In CS-HEA, the interaction between transformation and recrystallization affects the final microstructure after AFSD. To understand the interaction type, prediction of recrystallization kinetics in CS-HEA has been achieved using Johnson-Mehl-Avarami-Kolmogorov (JMAK) model [54–56]. The isothermal, sigmoidal-shaped recrystallization kinetics combining the nucleation and growth processes is characterized using JMAK model. The JMAK model is expressed using the equations below,

$$X_{rex} = 1 - \exp^{[-(\frac{t}{t_R})^n]} \quad (3)$$

$$t_R = t_0 \exp^{(\frac{Q_{RX}}{RT})} \quad (4)$$

where t is total time at higher temperature, t_R is the time required for 63% recrystallization, Q_{RX} is the activation energy for recrystallization, T is the processing temperature, and t_0 is pre-exponential factor. The activation energy considered for the present study is of steel due to similarity of alloying elements, for which the energy for recrystallization of rolled condition is 229.8 ± 28.0 kJ/mol [50]. The peak temperature predicted in Section 3.1 is 1210 ± 20 K for AFSD of CS-HEA. However, the temperature in the material varies in the range $0.6 - 0.9 T_m$ during the entire AFSD process [3,57]. Using Eqs. (3) and (4), and the parameter values mentioned above, the recrystallization kinetics for AFSD CS-HEA was predicted, the two temperatures were selected based on the maximum and minimum temperature during processing. Fig. 8(a) shows the sigmoidal curve of recrystallization fraction as a function of time for two temperature extremes of interest during AFSD. The figure reveals that the time for complete recrystallization is of the order of 10^{-3} sec at 1373 K and tens of seconds at 873 K. Since the AFSD of CS-HEA sustained for ~ 310 s, the deposited material is subjected to multiple thermal and deformation cycles during which the microstructure undergoes multiple recrystallization and grain growth cycles irrespective of the processing temperature. Such multiple thermal and deformation cycles result in a bi-modal microstructure with larger grown grains surrounded by fine recrystallized grains. Therefore, local deformation ratio and temperature are responsible for the discrepancy between experimental and JMAK kinetics during AFSD process.

The $\gamma \rightarrow \epsilon$ transformation temperature for CS-HEA is ~ 673 K [29,58] and to understand interaction of transformation and recrystallization kinetics, the recrystallization fraction is predicted for different temperatures using JMAK model. Fig. 8(b) shows the variation in recrystallization fraction with temperature for $t = 310$ s. As indicated in Fig. 8(b), the recrystallization in the material has not been started at the transformation temperature. Hence, the recrystallization process initiates only once the material transforms to γ -phase. Due to lack of simultaneity of transformation and recrystallization in CS-HEA, the interaction of both processes is weak.

As marked in the Fig. 7(c), most of the newly recrystallized grains are of high temperature metastable γ -phase. Once the γ -phase undergoes recrystallization and the temperature falls below the transformation temperature, $\gamma \rightarrow \epsilon$ martensitic transformation takes place. Non-recrystallized bigger grains with high dislocation density transformed to ϵ -phase whereas dislocation free grains remained as γ -phase. Generally, $\gamma \rightarrow \epsilon$ transformation is a stress induced transformation [59–62] and high dislocation density in the non-recrystallized grains stabilizes ϵ phase. Additionally, SFE plays a crucial role for $\gamma \rightarrow \epsilon$ transformation, as the formation of stacking faults on every other {1 1 1} plane results in the formation of HCP martensitic embryo in FCC [42]. The effective SFE of the material depends on the grain size as well (Eq. (2)) [42,63];

$$SFE_{eff} = n\rho(\Delta G_{chem}^{\gamma \rightarrow \epsilon} + E^{str} + \Delta G_{ex}^{\gamma \rightarrow \epsilon}) + 2\sigma^{\gamma/\epsilon} \quad (5)$$

where, ρ is the planar atomic density of {111} closed packed planes, $G_{chem}^{\gamma \rightarrow \epsilon}$ is the chemical driving force for the transformation, E^{str} is the strain energy barrier for the transformation, $\sigma^{\gamma/\epsilon}$ is the interfacial energy between the γ and ϵ phases, $\Delta G_{ex}^{\gamma \rightarrow \epsilon}$ is the excess free energy associated with parent phase, d is the grain size, k_1 and k_2 are constants having values 170.06 J/mol and 18.55 μm respectively [64]. According to Eqs. (2) and (5), the effective SFE of larger grains is lower as compared to smaller grains. Increase in the number of grain boundaries and phase

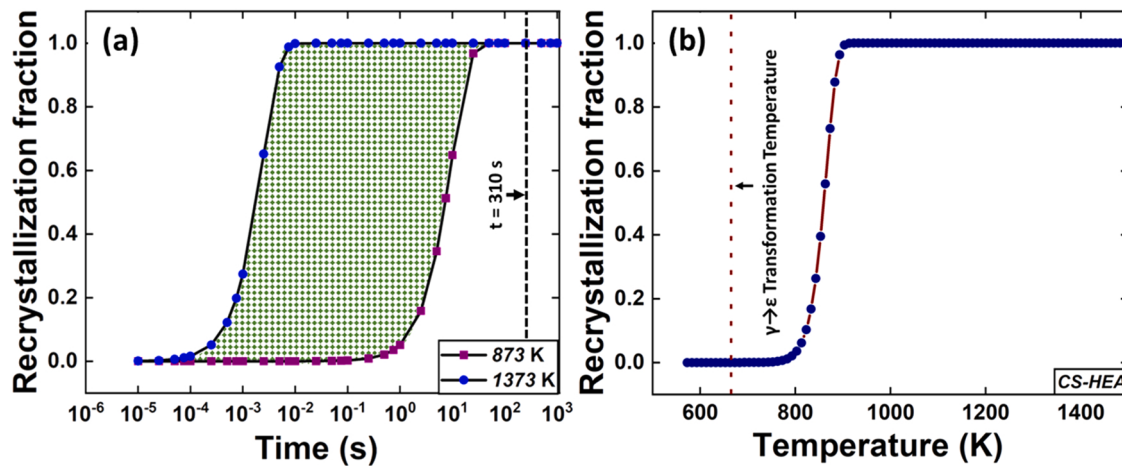


Fig. 8. (a) and (b) JMAK predicted recrystallization fraction variation with time and temperature respectively.

boundaries imparts additional back stresses within the grain, thereby increasing the energy required for stacking fault creation in smaller grains and thus causing the transformation difficult, whereas the transformation is apparently easier in bigger grains. Hence, the newly recrystallized grains remained as γ -phase during cooling due to additional energy requirement for transformation, whereas recrystallized and grown grains have transformed to ϵ -phase.

4.3. Work hardening model

The microstructure of the material is probabilistic, but the mechanical behavior is deterministic. The mechanical behavior of any material can be correlated to the microstructure of the material. CS-HEA is a TRIP enabled alloy and its deformation proceeds through multiple mechanisms which include slip, martensitic transformation, and deformation twinning. An analytical/numerical tool to predict the mechanical behavior based on the microstructure will be beneficial to determine the strength of the complex builds by avoiding tedious experimental routines. Such models facilitate part qualification of the builds for strength limiting design. In our previous study, simple four- and five-parameter empirical models [33,34] were developed to predict the tensile response as well as work hardening behavior of TRIP HEAs. As the deformation induced martensitic transformation is a function of microstructure and SFE, an attempt was made to correlate the model parameters with microstructure and SFE. Certain model parameters showed reasonable trends with the effective SFE of the alloy [33,34]. The five-parameter empirical model was applied to AFSD CS-HEA to predict the tensile stress-strain response as a function of the as-deposited microstructure.

The work hardening of TRIP HEA is divided in three stages (Fig. 6); Stage I is characterized by drop in hardening and it is associated with dominant slip activity. At a specific plastic strain, the slope of the work hardening curve changes and Stage II of deformation activates, which is associated with transformation and twinning along with non-basal slip in ϵ -phase. Four parameter hardening model [34] considered Stage II as a constant hardening phase, whereas five parameter hardening model assumed Stage II hardening with a slight increase in hardening with strain [33]. The modification in Stage II hardening is accommodated by introducing an additional parameter δ_2 to the four parameter hardening model. Further, deformation-induced martensitic transformation saturates with a resultant reduction in work hardening in Stage III which leads to diffuse necking and subsequent failure. The work hardening behavior can be replicated by using following empirical function [34],

$$\frac{d\sigma}{d\epsilon_p} = \beta_0 - \delta_1 \left\{ \frac{(\epsilon_p - \epsilon_i)}{(\epsilon_i + \epsilon_e)} \left| \tanh^{-1} \left(\frac{\epsilon_p - \epsilon_i}{\epsilon_i + \epsilon_e} \right) - \delta_2 \left(\frac{\epsilon_p - \epsilon_i}{\epsilon_i + \epsilon_e} \right) \right\}, \quad \left| \frac{(\epsilon_p - \epsilon_i)}{(\epsilon_i + \epsilon_e)} \right| < 1, \quad (6)$$

where σ is the flow stress, and ϵ_p is the true plastic strain that is equal to equivalent plastic strain under uniaxial loading. Eq. (6) is continuous, non-negative, and bounded in the interval $0 \leq \epsilon_p \leq 2\epsilon_i$. The ϵ_e term with a very small value of strain has been included to eliminate the unboundedness of argument of the inverse hyperbolic tangent function ($\frac{\epsilon_p - \epsilon_i}{\epsilon_i}$) at $\epsilon_p = 0, 2\epsilon_i$. In the current work, the model fits are obtained using $\epsilon_e = 0.001$. The parameter δ_1 controls the abruptness of $\frac{d\sigma}{d\epsilon_p}/\beta_0$ within $0 \leq \epsilon_p \leq \epsilon_i$, whereas parameter δ_2 controls the rate of gradual increase in the work hardening rate in stage II of deformation. β_0 is the hypothetical constant work hardening rate when $\delta = 0$. Integration of Eq. (6) gives the expression for σ as a function of ϵ_p as follows,

$$\sigma(\epsilon_p) = \beta_0 \epsilon_p \left\{ + \delta_1 \frac{(\epsilon_i + \epsilon_e)}{2} \left[\left((\tanh^{-1} \epsilon^*) (\epsilon^*)^2 + \epsilon^* - \ln \left| \frac{\sqrt{1 + \epsilon^*}}{\sqrt{1 - \epsilon^*}} \right| \right) \right. \right. \\ \left. \left. + \delta_2 (\epsilon^*)^2 \right], \quad (\epsilon_p < \epsilon_i) \right\} + C - \delta_1 \frac{(\epsilon_i + \epsilon_e)}{2} \left[\left((\tanh^{-1} \epsilon^*) (\epsilon^*)^2 \right. \right. \\ \left. \left. + \epsilon^* - \ln \left| \frac{\sqrt{1 + \epsilon^*}}{\sqrt{1 - \epsilon^*}} \right| \right) - \delta_2 (\epsilon^*)^2 \right], \quad (\epsilon_p \geq \epsilon_i) \quad (7)$$

where $\epsilon^* = \frac{(\epsilon_p - \epsilon_i)}{(\epsilon_i + \epsilon_e)}$ is the argument of the inverse hyperbolic tangent function in Eq. (6) and C is the integration constant, which is given by,

$$C = \sigma_0 - \delta_1 \frac{(\epsilon_i + \epsilon_e)}{2} \left[\left(\tanh^{-1} \left(\frac{(-\epsilon_i)}{(\epsilon_i + \epsilon_e)} \right) \right) \left(\frac{(-\epsilon_i)}{(\epsilon_i + \epsilon_e)} \right)^2 + \frac{(-\epsilon_i)}{(\epsilon_i + \epsilon_e)} \right. \\ \left. - \ln \left| \frac{\sqrt{1 - \frac{(-\epsilon_i)}{(\epsilon_i + \epsilon_e)}}}{\sqrt{1 + \frac{(-\epsilon_i)}{(\epsilon_i + \epsilon_e)}}} \right| \right) + \delta_2 \left(\frac{(-\epsilon_i)}{(\epsilon_i + \epsilon_e)} \right)^2 \quad (8)$$

Lloyd et al. [63] and Haridas et. al. [33,34] have shown that the model parameters can very well correlate to SFE of the material, given

Table 4

Parameters used for modelling of AFSD-CS-HEA, calculated using SFE of the material.

Parameters	S1	S3
ϵ_i	0.18	0.17
ϵ_e	0.001	0.001
β_0	3083	3145
d_1	1106	1106
d_2	0.27	0.27
σ_0	451	429
C	520.20	496.10

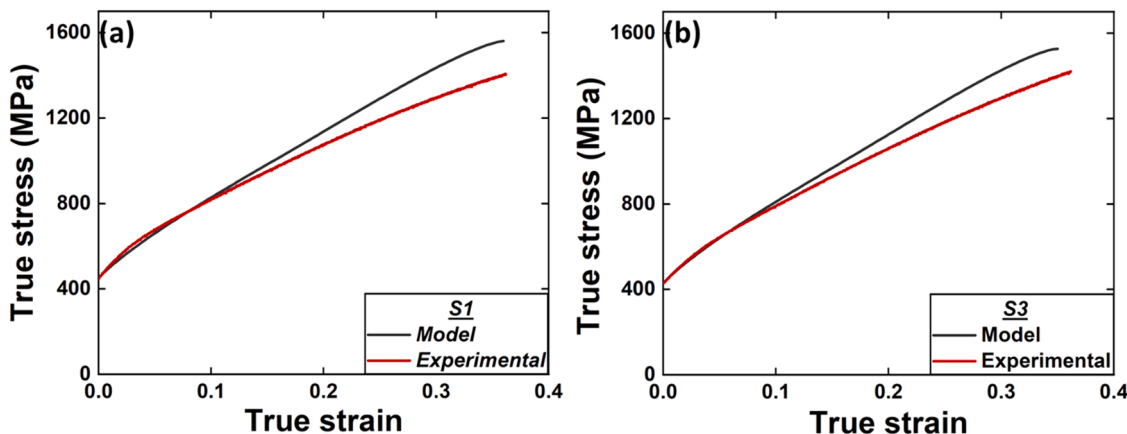


Fig. 9. Comparison of the tensile true stress-strain response obtained from model and experiments for samples (a) S1 and (b) S3, respectively.

by Eqs. (9) and (10). The SFE of the material depends on the chemical composition and microstructure of the material through the Eqs. (4) and (5). The SFE of the material is calculated for the microstructures of two different samples S1 and S3. The model parameters were obtained from their correlation with SFE [33,34], given in Table 4. The true stress-strain curve predicted using the Equation (7) and experimental curve are shown in Fig. 9(a) and (b) for samples S1 and S3, respectively.

$$\beta_0 = 16000 \times (SFE + 5.7)^{-0.6} \quad (9)$$

$$\epsilon_i = 0.0035 \times SFE + 0.15 \quad (10)$$

Fig. 9 reveals that the initial stages of the stress-strain behavior is similar for the both the samples. However, the model predicted higher hardening in both microstructures as compared to the experimental one. This could be due to the presence of ϵ -dominant microstructure in the as-deposited CS-HEA ($\sim 70\%$) which restricts persistent martensitic transformation.

5. Conclusions

This is the very first study that explores the novel AFSD – a solid-state AM process of a TRIP-enable HEA. A metastable TRIP HEA was deposited at different AFSD processing conditions. The microstructural evolution of AFSD CS-HEA at different processing conditions was studied using microscopic characterization at different length scales. CS-HEA is a dual phase alloy and the recrystallization kinetics during thermo-mechanical processing of CS-HEA was affected by the transformation kinetics. Following are the conclusions that can be drawn from the present study;

- Grain refinement in AFSD deposited CS-HEA ($\sim 3 \mu\text{m}$) as compared to the base material ($\sim 50 \mu\text{m}$) is due operation of high temperature restoration mechanism – discontinuous dynamic recrystallization in AFSD deposited CS-HEA.
- Heat input / peak temperature during AFSD of CS-HEA increases with increase in tool rotation rate and reducing tool traverse speed. The average grain size and high temperature FCC γ -phase fraction increases with increase in heat input / peak temperature during AFSD deposition.
- Deformation induced phase transformation and twinning in CS-HEA provided excellent tensile properties to the material with a yield strength of $450 \pm 20 \text{ MPa}$ and ductility of $50 \pm 5\%$.
- As CS-HEA is a low SFE material, discontinuous dynamic recrystallization is the controlling recrystallization mechanism. The deformation – recrystallization – grain growth cycle during AFSD resulted in discrepancy between experimentally evaluated and JMAK kinetics calculated recrystallization fraction of the alloy.

- The recrystallization kinetics of dual phase CS-HEA interacted with the transformation kinetics during processing. However, as the transformation and recrystallization temperatures do not overlap for CS-HEA, the microstructure is not affected significantly.

CRediT authorship contribution statement

Agrawal Priyanshi: Writing – original draft, Methodology, Investigation, Formal analysis, Data curation, Conceptualization. **Mishra Rajiv:** Writing – review & editing, Supervision, Resources, Project administration, Funding acquisition, Conceptualization. **Agrawal Priyanka:** Writing – review & editing, Investigation. **Haridas Ravi Sankar:** Writing – original draft, Methodology, Investigation, Formal analysis, Data curation, Conceptualization.

Declaration of Competing Interest

The authors declare that they have no known competing financial interests or personal relationships that could have appeared to influence the work reported in this paper.

Data availability statement

The raw/processed data required to reproduce these findings cannot be shared at this time, as the data also form part of an ongoing study.

Acknowledgments

The authors acknowledge the infrastructure and support of Center for Agile & Adaptive and Additive Manufacturing (CAAAM) funded through State of Texas Appropriation #190405–105-805008–220. The authors thank Materials Research Facility for access to microscopy facilities at the University of North Texas.

References

- D.D. Gu, W. Meiners, K. Wissenbach, R. Poprawe, Laser additive manufacturing of metallic components: Materials, processes and mechanisms, *Int. Mater. Rev.* 57 (2012) 133–164, <https://doi.org/10.1179/174328041Y.0000000014>.
- T. DebRoy, H.L. Wei, J.S. Zuback, T. Mukherjee, J.W. Elmer, J.O. Milewski, A.M. Beese, A. Wilson-Heid, A. De, W. Zhang, Additive manufacturing of metallic components – process, structure and properties, *Prog. Mater. Sci.* 92 (2018) 112–224, <https://doi.org/10.1016/j.pmatsci.2017.10.001>.
- R.S. Mishra, R.S. Haridas, P. Agrawal, Friction stir-based additive manufacturing, *Sci. Technol. Weld. Join.* 27 (2022) 141–165, <https://doi.org/10.1080/13621718.2022.2027663>.
- H.Z. Yu, R.S. Mishra, Additive friction stir deposition: a deformation processing route to metal additive manufacturing, *Mater. Res. Lett.* 9 (2021) 71–83, <https://doi.org/10.1080/21663831.2020.1847211>.
- S. Thapliyal, S. Shukla, L. Zhou, H. Hyer, P. Agrawal, M. Komarasamy, Y. Sohn, R.S. Mishra, Design of heterogeneous structured Al alloys with wide

- processing window for laser-powder bed fusion additive manufacturing, *Addit. Manuf.* 42 (2021), 102002, <https://doi.org/10.1016/j.addma.2021.102002>.
- [6] P. Agrawal, S. Thapliyal, S.S. Nene, R.S. Mishra, B.A. McWilliams, K.C. Cho, Excellent strength-ductility synergy in metastable high entropy alloy by laser powder bed additive manufacturing, *Addit. Manuf.* 32 (2020), 101098, <https://doi.org/10.1016/j.addma.2020.101098>.
- [7] R.S. Mishra, S. Thapliyal, Design approaches for printability-performance synergy in Al alloys for laser-powder bed additive manufacturing, *Mater. Des.* 204 (2021), 109640, <https://doi.org/10.1016/j.matdes.2021.109640>.
- [8] S. Thapliyal, P. Agrawal, P. Agrawal, S.S. Nene, R.S. Mishra, B.A. McWilliams, K. C. Cho, Segregation engineering of grain boundaries of a metastable Fe-Mn-Co-Cr-Si high entropy alloy with laser-powder bed fusion additive manufacturing, *Acta Mater.* 219 (2021), 117271, <https://doi.org/10.1016/j.actamat.2021.117271>.
- [9] A. Kumar Srivastava, N. Kumar, A. Rai Dixit, Friction stir additive manufacturing – an innovative tool to enhance mechanical and microstructural properties, *Mater. Sci. Eng. B Solid-State Mater. Adv. Technol.* 263 (2021), 114832, <https://doi.org/10.1016/j.msrb.2020.114832>.
- [10] P. Agrawal, R.S. Haridas, S. Yadav, S. Thapliyal, A. Dhal, R.S. Mishra, Additive friction stir deposition of SS316 stainless steel, *Addit. Manuf.* (n.d.).
- [11] A. Rollett, F. Humphreys, G.S. Rohrer, M. Hatherly, Recrystallization and Related Annealing Phenomena: Second Edition, 2004. <https://doi.org/10.1016/B978-0-08-044164-1.X5000-2>.
- [12] R.J. Griffiths, D. Garcia, J. Song, V.K. Vasudevan, M.A. Steiner, W. Cai, H.Z. Yu, Solid-state additive manufacturing of aluminum and copper using additive friction stir deposition: Process-microstructure linkages, *Materialia* 15 (2021), 100967, <https://doi.org/10.1016/j.mila.2020.100967>.
- [13] S. Mandal, A.K. Bhaduri, V. Subramanya Sarma, A study on microstructural evolution and dynamic recrystallization during isothermal deformation of a Ti-modified austenitic stainless steel, *Metall. Mater. Trans. A Phys. Metall. Mater. Sci.* 42 (2011) 1062–1072, <https://doi.org/10.1007/s11661-010-0517-7>.
- [14] F.J. Humphreys, Recrystallization mechanisms in two-phase alloys, *Met. Sci.* 13 (1979) 136–145, <https://doi.org/10.1179/msc.1979.13.3-4.136>.
- [15] U.U. Köster, Recrystallization involving a second phase, *Met. Sci.* 8 (1974) 151–160, <https://doi.org/10.1179/msc.1974.8.1.151>.
- [16] A. Mathevou, V. Massardier, D. Fabregue, P. Rocabois, M. Perez, A microstructurally based model for recrystallization in dual-phase steels, *Mettal. Mater. Trans. A Phys. Metall. Mater. Sci.* 51 (2020) 4228–4241, <https://doi.org/10.1007/s11661-020-05852-8>.
- [17] E.P. George, W.A. Curtin, C.C. Tasan, High entropy alloys: a focused review of mechanical properties and deformation mechanisms, *Acta Mater.* 188 (2020) 435–474, <https://doi.org/10.1016/j.actamat.2019.12.015>.
- [18] R.S. Mishra, R.S. Haridas, P. Agrawal, High entropy alloys – tunability of deformation mechanisms through integration of compositional and microstructural domains, *Mater. Sci. Eng. A* 812 (2021), 141085, <https://doi.org/10.1016/j.msea.2021.141085>.
- [19] Y. Zhang, T.T. Zuo, Z. Tang, M.C. Gao, K.A. Dahmen, P.K. Liaw, Z.P. Lu, Microstructures and properties of high-entropy alloys, *Prog. Mater. Sci.* 61 (2014) 1–93, <https://doi.org/10.1016/j.pmatsci.2013.10.001>.
- [20] P. Agrawal, S. Shukla, S. Gupta, P. Agrawal, R.S. Mishra, Friction stir gradient alloying: a high-throughput method to explore the influence of V in enabling HCP to BCC transformation in a γ-FCC dominated high entropy alloy, *Appl. Mater. Today* 21 (2020), 100853, <https://doi.org/10.1016/j.apmt.2020.100853>.
- [21] S. Shukla, T. Wang, M. Frank, P. Agrawal, S. Sinha, R.A. Mirshams, R.S. Mishra, Friction stir gradient alloying: a novel solid-state high throughput screening technique for high entropy alloys, *Mater. Today Commun.* 23 (2020), 100869, <https://doi.org/10.1016/j.mtcomm.2019.100869>.
- [22] R.S. Mishra, S.S. Nene, M. Frank, S. Sinha, K. Liu, S. Shukla, Metastability driven hierarchical microstructural engineering: Overview of mechanical properties of metastable complex concentrated alloys, *J. Alloy. Compd.* 842 (2020), 155625, <https://doi.org/10.1016/j.jallcom.2020.155625>.
- [23] H. Yu, J. Zhang, W. Fang, R. Chang, X. Bai, J. Yan, X. Zhang, B. Liu, F. Yin, A brief review of metastable high-entropy alloys with transformation-induced plasticity, *Mater. Sci. Technol. (U. Kingd.)* 36 (2020) 1893–1902, <https://doi.org/10.1080/02670836.2020.1851437>.
- [24] Z. Li, D. Raabe, Strong and ductile non-equiautomatic high-entropy alloys: design, processing, microstructure, and mechanical properties, *Jom* 69 (2017) 2099–2106, <https://doi.org/10.1007/s11837-017-2540-2>.
- [25] P. Agrawal, S. Gupta, S. Shukla, S.S. Nene, S. Thapliyal, M.P. Toll, R.S. Mishra, Role of Cu addition in enhancing strength-ductility synergy in transforming high entropy alloy, *Mater. Des.* 215 (2022), 110487, <https://doi.org/10.1016/j.matdes.2022.110487>.
- [26] S.S. Nene, M. Frank, P. Agrawal, S. Sinha, K. Liu, S. Shukla, R.S. Mishra, B. A. McWilliams, K.C. Cho, Microstructurally flexible high entropy alloys: Linkages between alloy design and deformation behavior, *Mater. Des.* 194 (2020), 108968, <https://doi.org/10.1016/j.matdes.2020.108968>.
- [27] A. Kumar, P. Dhekne, A.K. Swarnakar, M.K. Chopkar, Analysis of Si addition on phase formation in AlCoCrCuFeNiSix high entropy alloys, *Mater. Lett.* 188 (2017) 73–76, <https://doi.org/10.1016/j.matlet.2016.10.099>.
- [28] X. Liu, W. Lei, L. Ma, J. Liu, J. Liu, J. Cui, On the microstructures, phase assemblages and properties of Al0.5CoCrCuFeNiSix high-entropy alloys, *J. Alloy. Compd.* 630 (2015) 151–157, <https://doi.org/10.1016/j.jallcom.2014.11.085>.
- [29] S.S. Nene, M. Frank, K. Liu, S. Sinha, R.S. Mishra, B. McWilliams, K.C. Cho, Reversed strength-ductility relationship in microstructurally flexible high entropy alloy, *Ser. Mater. 154* (2018) 163–167, <https://doi.org/10.1016/j.scriptamat.2018.05.043>.
- [30] M. Frank, Y. Chen, S.S. Nene, S. Sinha, K. Liu, K. An, R.S. Mishra, Investigating the deformation mechanisms of a highly metastable high entropy alloy using in-situ neutron diffraction, *Mater. Today Commun.* 23 (2020), 100858, <https://doi.org/10.1016/j.mtcomm.2019.100858>.
- [31] S. Sinha, S.S. Nene, M. Frank, K. Liu, R.A. Lebensohn, R.S. Mishra, Deformation mechanisms and ductile fracture characteristics of a friction stir processed transformative high entropy alloy, *Acta Mater.* 184 (2020) 164–178, <https://doi.org/10.1016/j.actamat.2019.11.056>.
- [32] P. Agrawal, S. Thapliyal, S.S. Nene, R.S. Mishra, B.A. McWilliams, K.C. Cho, Excellent strength-ductility synergy in metastable high entropy alloy by laser powder bed additive manufacturing, *Addit. Manuf.* 32 (2020).
- [33] R.S. Haridas, P. Agrawal, S. Yadav, P. Agrawal, A. Gumaste, R.S. Mishra, Work hardening in metastable high entropy alloys: a modified five-parameter model, *J. Mater. Res. Technol.* 18 (2022) 3358–3372, <https://doi.org/10.1016/j.jmrt.2022.04.016>.
- [34] R.S. Haridas, P. Agrawal, R.S. Mishra, Modeling the work hardening behavior in metastable high entropy alloys, *Mater. Sci. Eng. A* 823 (2021), 141778, <https://doi.org/10.1016/j.msea.2021.141778>.
- [35] P. Agrawal, R.S. Haridas, S. Yadav, S. Thapliyal, S. Gaddam, R. Verma, R.S. Mishra, Processing-structure-property correlation in additive friction stir deposited Ti-6Al-4V alloy from recycled metal chips, *Addit. Manuf.* (2021).
- [36] R.S. Mishra, Z.Y. Ma, Friction stir welding and processing, *Mater. Sci. Eng. R. Rep.* 50 (2005) 1–78, <https://doi.org/10.1016/j.mser.2005.07.001>.
- [37] O.G. Rivera, P.G. Allison, L.N. Brewer, O.L. Rodriguez, J.B. Jordon, T. Liu, W. R. Whittington, R.J. Martens, Z. McClelland, C.J.T. Mason, L. Garcia, J.Q. Su, N. Hardwick, Influence of texture and grain refinement on the mechanical behavior of AA2219 fabricated by high shear solid state material deposition, *Mater. Sci. Eng. A* 724 (2018) 547–558, <https://doi.org/10.1016/j.msea.2018.03.088>.
- [38] C.J.T. Mason, R.I. Rodriguez, D.Z. Avery, B.J. Phillips, B.P. Bernarding, M. B. Williams, S.D. Cobbs, J.B. Jordon, P.G. Allison, Process-structure-property relations for as-deposited solid-state additively manufactured high-strength aluminum alloy, *Addit. Manuf.* 40 (2021), 101879, <https://doi.org/10.1016/j.addma.2021.101879>.
- [39] S. Palanivel, P. Nelaturu, B. Glass, R.S. Mishra, Friction stir additive manufacturing for high structural performance through microstructural control in an Mg based WE43 alloy, *Mater. Des.* 65 (2015) 934–952, <https://doi.org/10.1016/j.matdes.2014.09.082>.
- [40] K. Nishizawa, I. Taiji, *Eff. Alloy. Elemt. Stab. Epsil. Iron* 15 (1974) 499–506.
- [41] K. Ando, T. Omori, J. Sato, Y. Sutou, K. Oikawa, R. Kainuma, K. Ishida, Effect of alloying elements on fcc/hcp martensitic transformation and shape memory properties in Co-Al alloys, *Mater. Trans.* 47 (2006) 2381–2386, <https://doi.org/10.2320/matertrans.47.2381>.
- [42] G.B. Olson, M. Cohen, A general mechanism of martensitic nucleation: Part I. General concepts and the FCC → HCP transformation, *Metall. Trans. A* 7 (1976) 1897–1904, <https://doi.org/10.1007/BF02659822>.
- [43] C. Wang, C. Wang, J. Xu, P. Zhang, D. Shan, B. Guo, Interactive effect of microstructure and cavity dimension on filling behavior in micro coining of pure nickel, *Sci. Rep.* 6 (2016) 1–10, <https://doi.org/10.1038/srep23895>.
- [44] S. Sinha, S.S. Nene, M. Frank, K. Liu, P. Agrawal, R.S. Mishra, On the evolving nature of c/a ratio in a hexagonal close-packed epsilon martensite phase in transformative high entropy alloys, *Sci. Rep.* 9 (2019) 1–14, <https://doi.org/10.1038/s41598-019-49904-5>.
- [45] S. Fu, H. Bei, Y. Chen, T.K. Liu, D. Yu, K. An, Deformation mechanisms and work-hardening behavior of transformation-induced plasticity high entropy alloys by in-situ neutron diffraction, *Mater. Res. Lett.* 6 (2018) 620–626, <https://doi.org/10.1080/21663831.2018.1523239>.
- [46] S. Thapliyal, S.S. Nene, P. Agrawal, T. Wang, C. Morphew, R.S. Mishra, B. A. McWilliams, K.C. Cho, Damage-tolerant, corrosion-resistant high entropy alloy with high strength and ductility by laser powder bed fusion additive manufacturing, *Addit. Manuf.* 36 (2020), 101455, <https://doi.org/10.1016/j.addma.2020.101455>.
- [47] P. Agrawal, R.S. Haridas, S. Thapliyal, S. Yadav, R.S. Mishra, B.A. McWilliams, K. C. Cho, Metastable high entropy alloys: An excellent defect tolerant material for additive manufacturing, *Mater. Sci. Eng. A* 826 (2021), 142005, <https://doi.org/10.1016/j.msea.2021.142005>.
- [48] J.J. Jonas, X. Quelennec, L. Jiang, É. Martin, The Avrami kinetics of dynamic recrystallization, *Acta Mater.* 57 (2009) 2748–2756, <https://doi.org/10.1016/j.actamat.2009.02.033>.
- [49] D. Raabe, Recovery and Recrystallization: Phenomena. Physics, Models, Simulation, Fifth Edit, Elsevier, 2014, <https://doi.org/10.1016/B978-0-444-53770-6.00023-X>.
- [50] D. Ponge, G. Gottstein, Necklace formation during dynamic recrystallization: mechanisms and impact on flow behavior, *Acta Mater.* 46 (1998) 69–80, [https://doi.org/10.1016/S1359-6454\(97\)00233-4](https://doi.org/10.1016/S1359-6454(97)00233-4).
- [51] H.L. Yi, D. Wei, R.Y. Xie, Y.F. Zhang, H. Kato, Microstructure refinement of a transformation-induced plasticity high-entropy alloy, *Mater. (Basel)* 14 (2021) 1–14, <https://doi.org/10.3390/ma14051196>.
- [52] M. Kulakov, W.J. Poole, M. Militzer, The effect of the initial microstructure on recrystallization and austenite formation in a DP600 steel, *Mettal. Mater. Trans. A Phys. Metall. Mater. Sci.* 44 (2013) 3564–3576, <https://doi.org/10.1007/s11661-013-1721-z>.
- [53] S.A. Etesami, M.H. Enayati, Microstructural evolution and recrystallization kinetics of a cold-rolled, ferrite-martensite structure during intercritical annealing, *Mettal. Mater. Trans. A Phys. Metall. Mater. Sci.* 47 (2016) 3271–3276, <https://doi.org/10.1007/s11661-016-3528-1>.

- [54] W.A. Johnson, R.F. Mehl, Reaction kinetics in processes of nucleation and growth, *Trans. Am. Inst. Min. Metall. Eng.* Vol. 135 (1939) 416–442.
- [55] A.N. Kolmogorov, On the statistical theory of crystallization of metals, *Izv. Akad. Nauk SSSR, Ser. Mat.* 3 (1937) 355–359.
- [56] M. Avrami, Granulation, phase change, and microstructure kinetics of phase change. III, *J. Chem. Phys.* 9 (1941) 177–184, <https://doi.org/10.1063/1.1750872>.
- [57] H.Z. Yu, M.E. Jones, G.W. Brady, R.J. Griffiths, D. Garcia, H.A. Rauch, C.D. Cox, N. Hardwick, Non-beam-based metal additive manufacturing enabled by additive friction stir deposition, *Scr. Mater.* 153 (2018) 122–130, <https://doi.org/10.1016/j.scriptamat.2018.03.025>.
- [58] S. Gupta, P. Agrawal, S.S. Nene, R.S. Mishra, Friction stir welding of γ -fcc dominated metastable high entropy alloy: Microstructural evolution and strength, *Scr. Mater.* 204 (2021), 114161, <https://doi.org/10.1016/j.scriptamat.2021.114161>.
- [59] T.H. Ahn, S.B. Lee, K.T. Park, K.H. Oh, H.N. Han, Strain-induced ϵ -martensite transformation during nanoindentation of high-nitrogen steel, *Mater. Sci. Eng. A* 598 (2014) 56–61, <https://doi.org/10.1016/j.msea.2014.01.030>.
- [60] R.B. Figueiredo, F.L. Sicupira, L.R.C. Malheiros, M. Kawasaki, D.B. Santos, T. G. Langdon, Formation of epsilon martensite by high-pressure torsion in a TRIP steel, *Mater. Sci. Eng. A* 625 (2015) 114–118, <https://doi.org/10.1016/j.msea.2014.11.091>.
- [61] E. El-Danaf, S.R. Kalidindi, R.D. Doherty, Influence of grain size and stacking-fault energy on deformation twinning in fcc metals, *Metall. Mater. Trans. A Phys. Metall. Mater. Sci.* 30 (1999) 1223–1233, <https://doi.org/10.1007/s11661-999-0272-9>.
- [62] A. Kisko, R.D.K. Misra, J. Talonen, L.P. Karjalainen, The influence of grain size on the strain-induced martensite formation in tensile straining of an austenitic 15Cr-9Mn-Ni-Cu stainless steel, *Mater. Sci. Eng. A* 578 (2013) 408–416, <https://doi.org/10.1016/j.msea.2013.04.107>.
- [63] J.T. Lloyd, D.M. Field, K.R. Limmer, A four parameter hardening model for TWIP and TRIP steels, *Mater. Des.* 194 (2020), 108878.
- [64] P.H. Adler, G.B. Olson, W.S. Owen, Strain hardening of Hadfield manganese steel, *Metall. Mater. Trans. A* 17 (1986) 1725–1737.